Postprint **Formation of radiator structures in quartz veins - phase-field modeling of multi-crack sealing** by M. Späth, J. L. Urai, B. Nestler. Accepted for publication in Journal of Structural Geology on Mar 17, 2022. Original publication: https://doi.org/10.1016/j.jsg.2022.104576

Formation of radiator structures in quartz veins - phase-field modeling of multi-crack sealing

Michael Späth[a], Janos L. Urai[b], Britta Nestler[a,c]

[a]*Institute for Applied Materials (IAM-MMS), Karlsruhe Institute of Technology (KIT), Straße am Forum 7, 76131 Karlsruhe, Germany*
[b]*Institute of Tectonics and Geodynamics, RWTH Aachen University, Lochnerstraße 4-20, Aachen, Germany*
[c]*Institute of Digital Materials Science (IDM), Karlsruhe University of Applied Sciences, Moltkestraße 30, 76133 Karlsruhe, Germany*

Abstract

The present work showcases a comprehensive phase-field study on the formation of multi-crack-seal veins in quartz microstructures. The microstructure simulation framework Pace3D incorporates the modeling of both fracturing and sealing in polycrystalline rock systems, where crystallographic anisotropies, crack resistances and growth velocities of different facets are included in the energy density contributions. In a two grain system we exemplary show the formation of three different archetypes of radiators which are observed in natural quartz veins. We extend the phase-field studies to a polycrystalline host rock and investigate therein the effects of fracture aperture, presence of accessory minerals, and oblique opening trajectories with refracturing of fully and partially sealed veins on the occurring vein crystal morphology. Our results show that the shape of the forming grain boundaries

---

Corresponding author: Michael Späth
Email addresses: michael.spaeth@kit.edu (Michael Späth), j.urai@ged.rwth-aachen.de (Janos L. Urai), britta.nestler@kit.edu (Britta Nestler)

accepted manuscript

depends on the crystal orientation of the participating grains, the location of a fracture through the crystals, and the sealing state. Evolution of more pronounced radiator structures are found in simulation studies with increasing aperture. A broad spectrum of crystal structures which are frequently observed in natural quartz vein microstructures is reproduced in simulations using the combined crack-seal phase-field model.
Keywords: crack-seal veins, phase-field study, stretched crystals, fracture formation, serrated grain boundaries, radiator structures

1. Introduction

Fracture formation and fracture sealing are fundamental processes in rock systems in the earth crust. During deformation of the brittle crust fractures can form and create pathways for geothermal fluids. Depending on supersaturation and chemical potential of the aqueous fluids in open fractures dissolution or precipitation can occur and affect the rock properties as strength and permeability, which, for example, is of interest to basic geoscience or subsurface engineering (Cox et al. (1987); Sibson et al. (1988); McNamara et al. (2016); Almansour et al. (2020)). Syntectonic quartz and calcite veins frequently appear at low metamorphic grades in the upper and middle crust (Ramsay and Huber (1983); Passchier and Trouw (2005)), where coupled mechanical, chemical, and hydraulic processes lead to a wide range of micro- and macrostructures (Laubach et al. (2019)). The different crystal morphologies in the veins can provide information and help to reconstruct under which conditions they have formed (Boullier and Robert (1992); Fisher and Brantley (1992); Cox (2007); Bons et al. (2012)).

The seminal work of John Ramsay (Ramsay (1980)) firstly described the so-called crack-seal mechanism, where fracturing and sealing alternate numerous times. These crack-seal veins are ubiquitous in fractured rock and can show multiple fluid or solid inclusions inside the vein. When, instead of fracturing the vein, a new fracture forms delocalized in the host rock, the mechanism is called crack-jump (Caputo and Hancock (1998)). In the former case the vein is weaker than the host rock region (e.g. due to partial sealing), whereas in the latter case the host rock is weaker (Holland and Urai (2010); Virgo et al. (2014)).

In natural rocks a broad variability of different types of veins form with different characteristic crystal morphologies, for example syntaxial, ataxial, and antitaxial veins as schematically illustrated in Figure 1. The morphologies depend on the location of a fracture (localized, delocalized), opening trajectory of open fracture, vein filling mineral, and growth direction (Bons et al. (2012); Durney and Ramsay (1973)). In syntaxial and ataxial veins the filling mineral is the same as the host rock mineral. The crystals grow epitaxially or by nucleation on the fractured grains in the open fluid filled fracture. In syntaxial veins different crystals from both fracture walls connect in the vein center (e.g. intergranularly fractured grains) and may form a median line after repeated refracturing at the median line. In contrast, in ataxial veins crystals (which are cut through and are located at both fracture walls) reconnect over multiple refracturing events at different positions inside the vein without forming a grain boundary and median line. Characteristic crystal shapes in syntaxial veins are elongated blocky crystals, whereas atax-

ial veins show stretched crystals. In antitaxial veins the vein filling minerals are different than the host rock (e.g. calcite veins in mudrocks or shale) and they grow epitaxially on the vein from median zone outwards to an inert host rock, typically forming fibrous crystals when small opening increments occur.

Furthermore, the crystal morphology can be affected by a second precipitating phase, which can show different crystal growth rates (Becker et al. (2011)). Additionally the vein microstructure is influenced by the fracture type (inter- vs. transgranular vs. mixed type fracture), where different fracture types can exhibit different growth velocities. In limestone, for example, a growth rate difference between partially coated intergranular fractured grains (nucleation discontinuities (Lander et al. (2008))) and transgranular fractured grains can be present (Spruženiece et al. (2021, 2020)).

The majority of quartz crystals grow epitaxially on the host rock grains.

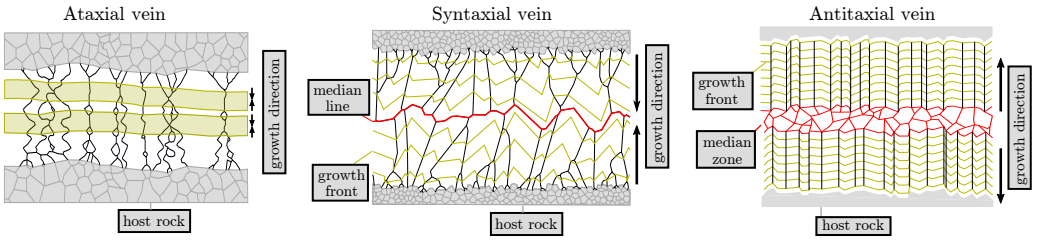

Figure 1: Schematic representation of different types of veins. On left: Ataxial vein with stretched crystals showing different growth fronts, which vary during different crack-seal events (in yellow). A median line is not visible. In Middle: Syntaxial vein with expitaxial growth on host rock showing elongated-blocky crystals with a distinct median line. Yellow lines indicate intermediate growth stages. On right: Antitaxial vein which grows from median zone towards inert host rock.

Both localized and delocalized fracturing can occur, resulting thin or thick

vein bundles. Stretched crystals, which form during localized refracturing, show a wide spectrum of crystal morphologies in natural veins, where the grain boundaries can be serrated (radiator microstructures) or flat and host rock inclusions can be present. Each crack-seal event produces a new radiator, whereas spaced bands and inclusions show a regular pattern and can indicate the stress states during the time of fracture sealing (Renard et al. (2005)). Figure 2 illustrates different crystal morphologies in a quartz microstructure from Portugal near Carrapateira, where different radiator microstructures are present.

Besides microscopic analysis of natural veins hydrothermal flow-through ex-

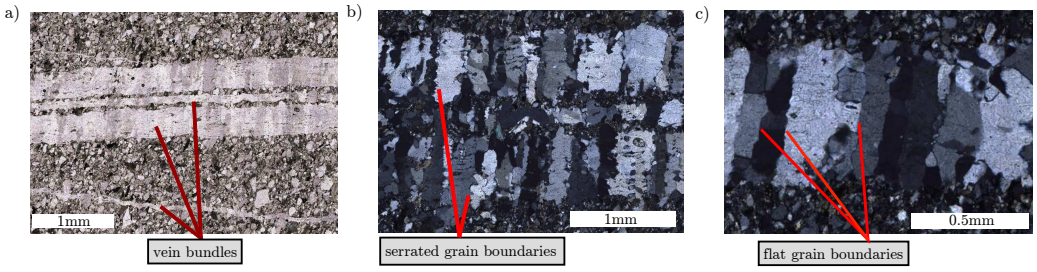

Figure 2: Natural ataxial quartz veins from Portugal near Carrapateira. Light microscopic images are taken under a) plane and b),c) crossed polarizers. a) Thick and thin vein bundles embedded in host rock. b) and c) show flat and serrated grain boundaries between the stretched crystals.

periments of quartz or in quartz rich rocks (e.g. Lander et al. (2008); Thomas et al. (1949); Cecil and Heald (1971); Okamoto et al. (2010); Okamoto and Sekine (2011); Busch et al. (2021)) enable a better understanding of how crystals form (e.g. facets, overgrowth of nucleation discontinuities) and how they interact during the precipitation under various conditions in polycrystalline environments. Okamoto and Sekine (2011) for example investigated

the syntaxial quartz growth in open fractures and observed growth competition between differently oriented crystals and a growth termination against crystals from the opposite fracture wall. However, these crystal growth experiments were (so far) limited to single seal processes or growth in open voids.

Moreover, computational modeling of fracture sealing processes has become an important methodology to provide further insights on crystal shape evolution or fluid connectivity during vein formation. One of the first models of crystal growth in open fractures was presented by Urai et al. (1991), where the relationship between wall rock surface together with opening increment to the vein crystal shape was tested in antitaxial veins. This work was extended with sharp interface models like *Facet* by Zhang and Adams (2002) or *Vein Growth* by Bons (2001); Hilgers et al. (2001); Nollet et al. (2005), where the effects of different factors (e.g. aperture, opening trajectory) on the crystal structure in antitaxial veins were demonstrated.

Furthermore, the cellular automaton program *Prism2D* (Lander et al. (2008)) has been applied to single and polygrain systems (Lander et al. (2008)) and syntaxial and ataxial veins in quartz (Lander and Laubach (2015)) and dolostone (Gale et al. (2010)). Lander and Laubach (2015) calibrated their model with laboratory growth experiments and incorporated effects of periodic bond chain theory (Hartman and Perdok (1955)). They showed the formation of crystal bridges and stretched crystals in veins with repeated refracturing.

The formation of fractures in geological structures has been modeled with several approaches, for example Discrete Element Method (DEM) (Virgo

et al. (2014, 2013, 2016)), Boundary Element Method (BEM) (Zhang and Jeffrey (2014)), Extended Finite Element Method (XFEM) (Wang et al. (2018)), Peridynamics (Ha and Bobaru (2010)), or Linear Elastic Fracture Mechanics (LEFM) (Paluszny et al. (2020)). For a detailed discussion about the different approaches we refer to the review article of Mohammadnejad et al. (2018).

The phase-field method is widely used in material science for modeling phase transition processes and has developed in recent years as a potent tool in modeling fracturing and fracture sealing processes in geological environments. The method uses a mathematical model for the representation of the interfaces between different phases (e.g. different grains) in a diffuse manner. This diffuse interface approach enables the method to elegantly treat moving boundary problems without the necessity of expensive remeshing or interface tracking algorithms. The phase-field method has been applied in geological systems to dissolution (Xu and Meakin (2008); Ray et al. (2019); Bringedal et al. (2020); Prajapati et al. (2021)) or precipitation processes in open fractures and reservoirs. Different types of minerals which frequently appear in the earth crust have been investigated as calcite (veins: Spruženiece et al. (2021, 2020); Prajapati et al. (2017); Späth et al. (2021); reservoirs: Prajapati et al. (2018)) or quartz (veins: Ankit et al. (2015); Wendler et al. (2016) or reservoirs: Prajapati et al. (2018, 2020)) in 2D or 3D. The phase-field method enables the incorporation of different effects in the numerical models as prescription of faceted crystal growth, different growth velocity between rough and faceted growth (e.g. PBC theory (Hartman and Perdok (1955))),

and different growth velocities between fracture types and can be calibrated to laboratory crystal growth experiments (Wendler et al. (2016); Prajapati et al. (2020)).

Furthermore, the phase-field method is established in fracture formation modeling and has been applied to elastic and inelastic materials (Ambati et al. (2015)) with small and large deformations (Miehe et al. (2016)) varying from single phase to polycrystalline systems (Nguyen et al. (2017); Prajapati et al. (2020)) while also being able to include effects of corrosion (Nguyen et al. (2018)) or hydraulic fracturing (Mikelić et al. (2015)). There is an extensive literature available and we further refer exemplary to review articles of Ambati et al. (2015) and Heider (2021).

Even though previous studies focused on formation of fractures in geological structures or computationally investigated crystal growth in open fractures a combined simulation of the crack-seal mechanism at grain scale in a uniform software solution has not been presented so far.

In the present work we build upon the previous works of vein formation, while we combine the modeling of both fracture formation and crystal growth. The aim of this work is to provide further insight in the crack-seal mechanism and the formation of radiator microstructures. We focus on veins in quartz microstructures in which the sealed vein is refractured multiple times (multi-crack-seal veins). In our studies we include and systematically investigate the effects of different host rock compositions, varying fracture apertures, and varying opening trajectories on the crystal morphology.

2. Methods

In this work we utilize the phase-field method for modeling both the process of fracturing as well as fracture sealing of polycrystalline rock microstructures. Crystallographic anisotropies are incorporated in all processing steps.

2.1. Multiphase-field model for fracture formation

Here, we briefly recapitulate the utilized phase-field model for crack propagation from Prajapati et al. (2020), which has been utilized for fracture formation in quartz microstructures and is used in the present work. The model is described in detail in Prajapati et al. (2020), where the numerical treatment and representative applications are discussed.

We consider a computational domain Ω, which comprises N phase-field order parameters ϕ_α. They are collectively represented by the phase-field vector $\boldsymbol{\phi}(\boldsymbol{x},t) = \{\phi_1(\boldsymbol{x},t), \dots \phi_{N-1}(\boldsymbol{x},t), \phi_c(\mathbf{x},t)\} = \{\boldsymbol{\phi}_\mathrm{s}, \phi_\mathrm{c}\}$, where non-bold symbols refer to scalar quantities and bold symbols indicate vector quantities. The first $N-1$ phases correspond to solid phases (grains) and the last phase denotes the crack phase. Each phase-field order parameter $\phi_\alpha(\boldsymbol{x},t) \in [0,1]$ describes the volume-fraction of a particular solid phase or crack phase α at spatial position $\boldsymbol{x}$ and time t, whereas the each solid phase can be assigned with individual material properties (e.g. orientation, stiffness). In contrast to sharp interface methods the domain between different phases is characterized by a diffuse region of finite width, in which the order parameter $\phi_\alpha(\boldsymbol{x},t)$ continuously changes from 0 outside of a phase α to 1 inside. The solid phases represent mineral grains, whereas the crack phase ϕ_c characterizes the material degradation, for example $\phi_c = 1$ represents a fully damaged material and

$\phi_c = 0$ a fully intact material. At each computational grid point, the summation constraint over all occurring order parameters is ensured: $\sum_{\alpha}^{N} \phi_\alpha = 1$. The length scale parameter ϵ_c controls the crack interface width.

The temporal and spatial evolution of the crack phase-field is described by the Allen-Cahn equation (Cahn and Allen (1977)) in terms of a variational derivative of the free energy functional which is given as

$$\frac{\partial \phi_{\mathrm{c}}(\boldsymbol{x}, t)}{\partial t} = -\frac{M_{\mathrm{c}}}{\epsilon_c} \frac{\delta \mathcal{F}_{\mathrm{c}}(\boldsymbol{\phi}, \boldsymbol{\nabla}\phi_{\mathrm{c}}, \boldsymbol{\varepsilon})}{\delta \phi_{\mathrm{c}}}, \tag{1}$$

where M_{c} is a positive mobility, which is set constant in this work. The total free energy functional $\mathcal{F}_{\mathrm{c}}$ of a domain Ω is based on Griffith's criterion (Griffith (1921); Francfort and Marigo (1998)) and is denoted as

$$\mathcal{F}_{\mathrm{c}}(\boldsymbol{\phi}, \boldsymbol{\nabla}\phi_{\mathrm{c}}, \boldsymbol{\varepsilon}) = \int_{\Omega} \frac{G_{\mathrm{c}}(\boldsymbol{\phi}, \boldsymbol{\nabla}\phi_{\mathrm{c}})}{2} \left[\frac{1}{\epsilon_{\mathrm{c}}} \phi_{\mathrm{c}}^2 + \epsilon_{\mathrm{c}} |\boldsymbol{\nabla}\phi_{\mathrm{c}}|^2 \right] + f_{\mathrm{el}}(\boldsymbol{\varepsilon}, \boldsymbol{\phi}) \mathrm{d}\Omega. \tag{2}$$

Here, the effective crack resistance is given by G_{c} and the effective strain energy density by f_{el}. $\boldsymbol{\varepsilon}$ represents the elastic strain tensor (small strain theory), and $\boldsymbol{\nabla}\phi_{\mathrm{c}}$ is the gradient of ϕ_{c}. The energy of a propagating fracture is mapped in a regularized manner by the terms in the big bracket, which comprise the single side well-type potential term ϕ_{c}^2 and the gradient term $|\boldsymbol{\nabla}\phi_{\mathrm{c}}|^2$.

The effective crack resistance G_{c} is volumetrically averaged by the phase-inherent crack resistances $G_{\mathrm{c}}^{\alpha}(\boldsymbol{\nabla}\phi_{\mathrm{c}})$. For modeling anisotropic brittle fracture formation in polycrystalline quartz microstructures, Prajapati et al. (2020) introduced an anisotropy of the crack resistance:

$$G_{\mathrm{c}}^{\alpha}(\boldsymbol{\nabla}\phi_{\mathrm{c}}) = G_{\mathrm{c},0}^{\alpha} \Big[f_{\mathrm{a},x}^{\alpha} \Big(n_{\mathrm{c},x}^{\alpha}(\boldsymbol{\nabla}\phi_{\mathrm{c}}) \Big)^2 + f_{\mathrm{a},y}^{\alpha} \Big(n_{\mathrm{c},y}^{\alpha}(\boldsymbol{\nabla}\phi_{\mathrm{c}}) \Big)^2 + f_{\mathrm{a},z}^{\alpha} \Big(n_{\mathrm{c},z}^{\alpha}(\boldsymbol{\nabla}\phi_{\mathrm{c}}) \Big)^2 \Big].$$

The crack resistance in x, y, and z-direction can be degraded with the anisotropy factors $f^{\alpha}_{\mathrm{a},d} \in [0,1], d = x, y, z$. Since quartz exhibits a reduced fracture toughness in the basal plane (a-axes) (Norton and Atkinson (1981); Ferguson et al. (1987)) we adjust $f^{\alpha}_{\mathrm{a},x} = f^{\alpha}_{\mathrm{a},z} \in (0,1)$ and set $f^{\alpha}_{\mathrm{a},y} = 1$, whereas the x and z-direction correspond to the basal plane and the y-direction to the c-axis. The factor $\mathrm{f}_{\mathrm{aniso,a}} = f^{\alpha}_{\mathrm{a},x}/f^{\alpha}_{\mathrm{a},y}$ describes the weakness of the a-axis to the c-axis in the 2D case. The phase-inherent crack resistance is rotated according to crystallographic orientation of each quartz grain. In Figure 3a the anisotropic crack resistance is plotted for different anisotropy factors.
In the present work we assume that the precipitation process occurs on a

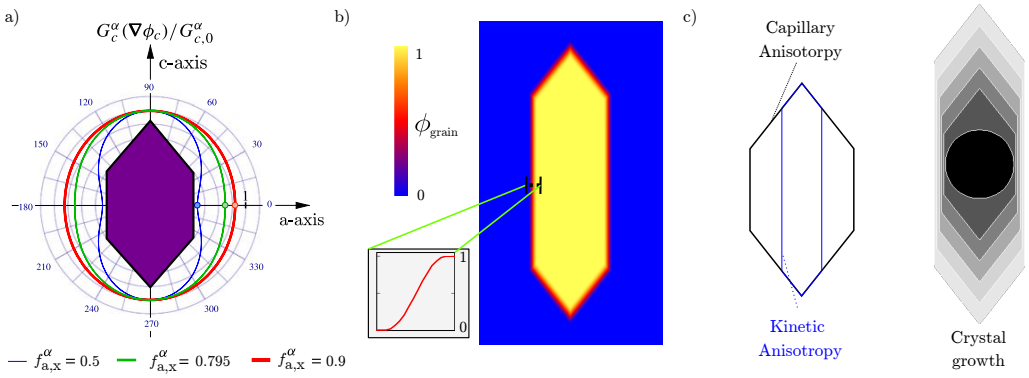

Figure 3: a) Anisotropic crack resistance of the quartz crystal (adapted from Prajapati et al. (2020)). Plot shows different anisotropy factors. b) Phase-field order parameter decreases continuously from 1 (inside of grain) to 0 (outside of grain). c) On left: Shape of capillary in kinetic anisotropies. On right: Growth of quartz crystal from a sphere. The temporal evolution is highlighted from black to light gray.

slower timescale than the fracture formation. Therefore, in our simulations crystal growth does not occur during the crack propagation and we formulate

the evolution of solid phases as

$$\frac{\partial \phi_\alpha}{\partial t} = -h_\mathrm{s}^\alpha(\boldsymbol{\phi}) \frac{\partial \phi_\mathrm{c}}{\partial t} \qquad \text{for} \quad \alpha = 1, .., N-1, \tag{3}$$

with the interpolation function $h_\mathrm{s}^\alpha = \phi_\alpha / \sum_\beta^{N-1} \phi_\beta$. Moreover, effects of crack sealing are not considered during the fracture formation, therefore $\dot{\phi}_\mathrm{c} \geq 0$ is ensured (Kuhn and Müller (2010)). The strain energy density f_el is volumetrically interpolated with the phase-inherent strain energy densities. In order to avoid non-physical fracture formation in compressive stress states we apply the spectral decomposition of Miehe et al. (2010) where the strain energy density is additively decomposed into positive and negative parts.

The simulation studies on fracture formation are performed on an equidistant, orthogonal grid. Due to the diffuse interface approach of the phase-field method a complex discretisation is not necessary. The phase-field evolution equation (1) is solved temporally with an explicit Euler scheme and spatially with a second order accurate central difference scheme (Schneider et al. (2016)). The mechanical fields are implicitly computed on a rotated staggered grid with a finite element (FE) discretisation with linear elements (full integration). The displacement fields are computed by solving the static momentum balance $\boldsymbol{\nabla} \cdot \boldsymbol{\sigma} = \mathbf{0}$, while the mechanical jump conditions are ensured in the diffuse solid interface regions (Schneider et al. (2016)). The evolution of the crack phase-field (eq. (1)) is computed with the input from the mechanical fields. We apply the mechanical loading incrementally, whereas after the crack phase-field reaches a steady state a new loading increment is applied. In the present work the simulations are performed in 2D under plane strain condition which corresponds to stress conditions in sub-surface environments. The utilized material properties are given in Table 1, which also

Table 1: Values of phase-field model parameters used in fracture formation models adapted from Prajapati et al. (2020)

Model parameter	Value
Grid spacing Δx	0.5μm
Time-step width Δt	1.0
Crack interface width parameter ε_c	4Δx
Fracture toughness along c-axis $K_{I,c}^{c\text{-axis}}$	2.4 MN $m^{-3/2}$ (Norton and Atkinson (1981))
Fracture toughness along a-axis $K_{I,c}^{a\text{-axis}}$	2.14 MN $m^{-3/2}$ (Ferguson et al. (1987))
Youngs modulus E	99.45 GPa (Heyliger et al. (2003))
Poisson ratio ν	0.06 (Heyliger et al. (2003))
Anisotropy factor $f_{aniso,a}$	0.795

have been applied in Prajapati et al. (2020).

2.2. Multiphase-field model for crystal growth

We apply a multiphase-field model for investigating crystal growth in open fractures based on the work of Nestler et al. (2005). The utilized model is briefly described here, whereas for a more detailed description of the model equations we refer to e.g. Spruženiece et al. (2021); Ankit et al. (2015); Wendler et al. (2016); Prajapati et al. (2020).

Similarly as in the fracture formation model the evolution of the phase-field order parameters is based on the minimization of the free energy, which is denoted as

$$\mathcal{F}(\boldsymbol{\phi}, \boldsymbol{\nabla\phi}) = \int_\Omega \Big[\epsilon a(\boldsymbol{\phi}, \nabla\boldsymbol{\phi}) + \frac{1}{\epsilon}\omega(\boldsymbol{\phi}) + f_{\text{bulk}}(\boldsymbol{\phi})\Big] \mathrm{d}\Omega = \mathcal{F}_{\text{intf}} + \mathcal{F}_{\text{bulk}}. \quad (4)$$

The phase-field vector $\boldsymbol{\phi}(\boldsymbol{x},t) = [\phi_1(\boldsymbol{x},t),\ldots,\phi_N(\boldsymbol{x},t)]$ comprises the N phase-fields $\phi_\alpha(\boldsymbol{x},t)$. Each phase-field $\phi_\alpha(\boldsymbol{x},t)$ represents a crystal or liquid phase, where a diffuse region of finite width describes the interface between different phases (Fig. 3b), which is controlled by ϵ. The interfacial energy density contributions in eq. (4) are represented by the gradient energy density $\epsilon a(\boldsymbol{\phi}, \nabla\boldsymbol{\phi})$ and the potential free energy density $\frac{1}{\epsilon}w(\boldsymbol{\phi})$, whereas $f_{\text{bulk}}(\boldsymbol{\phi})$ indicates the bulk free energy density. We use a multi-obstacle potential energy density (e.g. (Prajapati et al. (2017))) in this work. The gradient energy density is given by

$$\epsilon a(\boldsymbol{\phi}, \nabla(\boldsymbol{\phi})) = \epsilon \sum_{\alpha<\beta}^{N} \gamma_{\alpha\beta} a_{\alpha\beta}^2(\boldsymbol{\phi}, \nabla\boldsymbol{\phi}) |\mathbf{q}_{\alpha\beta}|^2, \tag{5}$$

where $\gamma_{\alpha\beta}$ is the surface energy density of the α-β interface and $\mathbf{q}_{\alpha\beta} = \phi_\alpha \boldsymbol{\nabla}\phi_\beta - \phi_\beta \boldsymbol{\nabla}\phi_\alpha$ is the interface normal vector. For modeling an anisotropic growth of crystals the gradient energy density function can be adapted the factor $a_{\alpha\beta}$. In the present work we use faceted type anisotropy for the crystal growth with a piecewise defined anisotropic surface energy function

$$a_{\alpha\beta}(\boldsymbol{\phi}, \nabla\boldsymbol{\phi}) = \max_{1\leq k\leq \eta_{\alpha\beta}} \left\{\hat{\boldsymbol{n}} \cdot \eta_{k,\alpha\beta}\right\}, \tag{6}$$

with the interface normal vector $\hat{\boldsymbol{n}} = \frac{\mathbf{q}_{\alpha\beta}}{|\mathbf{q}_{\alpha\beta}|}$ and the $n_{\alpha\beta}$ corners of the Wulff shape.

The temporal evolution of each phase-field ϕ_α is described with the variational derivative of the energy functional (eq. (4)) and is denoted by

$$\frac{\partial\phi_\alpha}{\partial t} = -\frac{1}{N\epsilon} \sum_{\alpha\neq\beta}^{N} \left[M_{\alpha\beta}(\hat{\boldsymbol{n}}) \left(\frac{\delta\mathcal{F}_{\text{intf}}}{\delta\phi_\alpha} - \frac{\delta\mathcal{F}_{\text{intf}}}{\delta\phi_\beta} - \frac{8\sqrt{\phi_\alpha\phi_\beta}}{\pi} \left(\frac{\delta\mathcal{F}_{\text{bulk}}}{\delta\phi_\beta} - \frac{\delta\mathcal{F}_{\text{bulk}}}{\delta\phi_\alpha} \right) \right) \right]. \tag{7}$$

We use the approach of Steinbach (2009) to obtain correct interface kinetics corresponding to the utilized obstacle-type potential and also avoid interpolation difficulties of the mobility in multiphase regions. The mobility coefficient of the α-β interface is given by

$$M_{\alpha\beta}(\hat{\boldsymbol{n}}) = M^0_{\alpha\beta} a^{\text{kin}}_{\alpha\beta}(\hat{\boldsymbol{n}}), \tag{8}$$

where the kinetic coefficient is given by $M^0_{\alpha\beta}$ and $a^{\text{kin}}_{\alpha\beta}(\hat{\boldsymbol{n}})$ represents the kinetic anisotropy term. Incorporating the feature that rough crystal surface can grow faster than fully faceted surface (PBC theory) the kinetic anisotropy is modeled with the approach of Wendler et al. (2016)

$$a^{\text{kin}}_{\alpha\beta}(\hat{\boldsymbol{n}}) = \left(1 + \delta \left(\max_k \left\{\hat{\boldsymbol{n}} \cdot \eta_{k,\alpha\beta}\right\} - \max_{k-1} \left\{\hat{\boldsymbol{n}} \cdot \eta_{k,\alpha\beta}\right\}\right)\right) \max_k \left\{\hat{\boldsymbol{n}} \cdot \eta_{k,\alpha\beta}\right\}. \tag{9}$$

The multiphase-field model equations for fracture formation and crystal growth are implemented in the inhouse solver package PACE3D v.2.5.1 (Parallel Algorithms for Crystal Evolution in 3D), which is written in language C. For implementation details and a description of optimisation algorithms, we refer interested readers to Hötzer et al. (2018).

In the present work we use for the crystal growth a constant chemical driving force which assumes continuous inflow of constant supersaturated fluid and slow attachment kinetics compared to flow rate.

Moreover, in order to reduce computational cost for the fracture formation and crystal growth in polycrystalline rock structures we perform all simulations exclusively in 2D. However, the general phase-field model with 3D crystal shapes and anisotropies as well as 3D fracture modeling is implemented in the PACE3D framework, but requires huge computing times.

The 2D models are capable to capture most features of the microstructural evolution (Spruženiece et al. (2021); Ankit et al. (2015)), however an out-of-plane growth and full rotation of the crystal orientations is not taken into account.

Even though quartz exhibit a broad spectrum of crystal habits (Goldschmidt (1922)) we use a prismatic bipyramidal crystal shape which is commonly observed in nature and therefore utilize the proposed phase-field parameters and 2D vector set for the kinetic and capillary anisotropy from Wendler et al. (2016) (Fig. 3b,c). The parameters used in the simulations are given in Table 2.

In all crystal growth simulations we set a zero-gradient boundary condition at the lower and upper boundary and an anisotropic boundary condition at the right and left boundary to ensure that the shape of the crystal facets is maintained precisely at the boundaries.

3. Results

3.1. Formation of serrated grain boundaries in a two-grain system

In this section we analyze the formation of different types of serrated grain boundaries (radiator structures) in a two quartz grain setup in which the orientation of the grains is varied in three representative cases. The initial setup (220x200Δx) with an initial crack on the left side (length 20Δx) is depicted in Figure 4a. The insertion of an initial crack corresponds to an initialization of the crack outside of the simulation domain. We simulate two consecutive crack-seal events. In each of the crack steps the lower fracture

Table 2: Values of phase-field model parameters used in crystal growth simulations adapted from Wendler et al. (2016)

Model parameter	Value	Dim. value
Grid spacing Δx	0.5	0.5 μm
Time-step width Δt	0.000625	0.725 s
Length scale parameter ϵ	4Δx	2μm
Interfacial energy density γ_{sl}	1.0	0.36 J m^{-2}
Interfacial energy density γ_{ss}	1.72	0.62 J m^{-2}
Higher order parameter $\gamma_{\alpha\beta\delta}$	12.0	4.32 J m^{-2}
Mobility of quartz grains to liquid $M^0_{\text{quartz-liq.}}$	1.0	2.39 $\times 10^{-15}$m^{4}J^{-1}s^{-1}
δ	85	
Bulk energy density for crystals f^{α}_{bulk}	-0.294	1.059$\times 10^5$ J m^{-3}

wall is shifted downwards (parallel to the loading vector) after the rock specimen is fractured to get an aperture of 60Δx. Then, the crystal growth is initiated until the fracture is fully sealed. For the second crack-seal cycle, a new initial crack is inserted on the left side again. For the second fracturing event, two different positions are considered at which the crack occurs: (I) The crack is located in the vein center and (II) in the upper half of the vein. The two different processing routes are analysed and discussed.

In the first simulation series both crystals have the same orientation and the c-axis lies in vertical direction (Fig. 4b). The fracture cuts straight through the grains while following the weaker a-axis. Then, after the crack opening, the crystals on both side of the fracture grow and reconnect in the center of the fracture. Since the fast growing c-axis of both crystals has no axial tilt

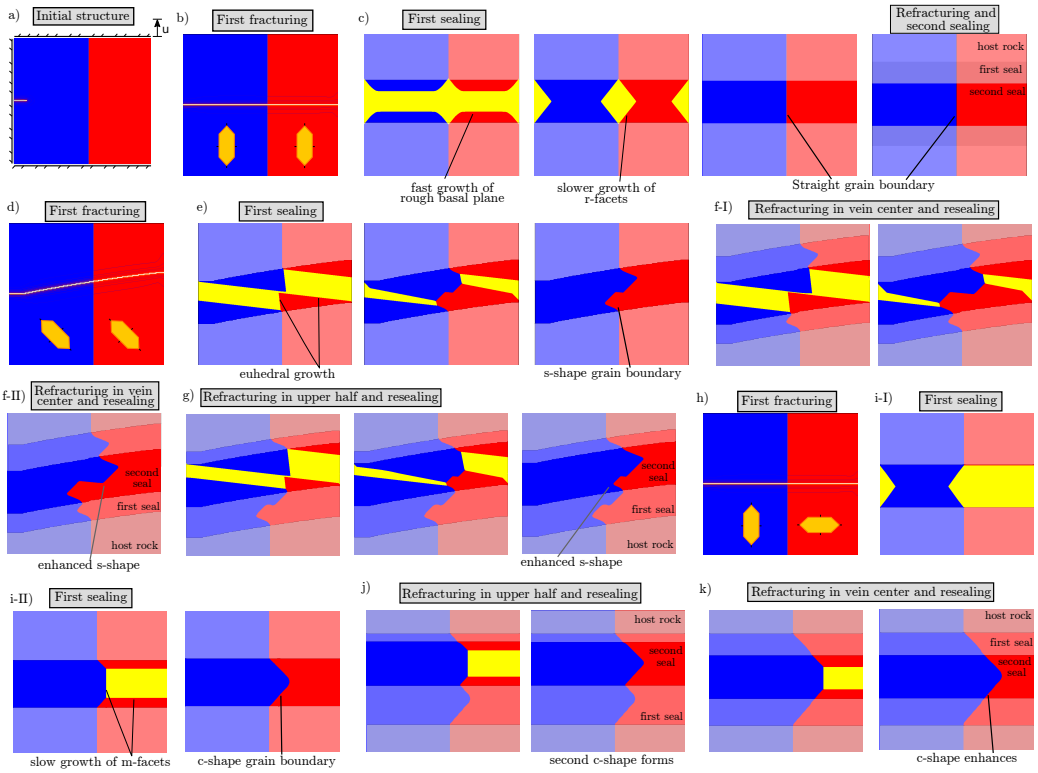

Figure 4: Evolution of radiators in a two grain setup. a) Initial structure with displacement boundary condition ($\mathbf{u}$) for mode I loading. b)-c) Fracturing and resealing of two parallel oriented grains with vertical c-axis alignment forming flat grain boundaries. d)-g) Two crack-seal events with two parallel grains with 45° tilt and h)-k) two grains horizontally and vertically aligned. The second crack is initiated both in the vein center and in the upper half of the sealed vein. In e)-g) s-shape radiators form and in h)-k) c-shape radiators form. The initial host rock is highlighted in light gray, the precipitated mineral during the first sealing is highlighted in darker gray, and the liquid phase in yellow.

no radiator forms in the first and second crack-seal cycle independently on the location of the second crack (Fig. 4c).

In the second case both crystals have an anti-clockwise axial tilt of 45° (Fig. 4d). Here, the fracture cuts the two grain specimen with a lower an-

gle than the prescribed anisotropy, which results from the interplay of the highest driving force of mode I loading (at crack tip) and the direction of the weakest crack resistance (see discussion in Prajapati et al. (2020)). During the sealing (stage where euhedral growth is reached in Fig. 4e) the crystal fragments with a fast growing c-axis in direction of the open fracture can expand over their neighboring crystal fragment where a slower growing r-facet grows, which results in a meandering/s-shape radiator. During the second crack-seal cycle (Fig. 4f,g) the s-shape radiator becomes more pronounced, modulated by the location of the second initial crack.

In the third case the c-axis of the blue grain is vertical and the red grain is horizontal (Fig. 4h). The fracture runs through the digital rock following the weak a-axis of the blue grain. Then, the fracture also cuts through the red grain without a deflection as a result of the interplay between weakest G_c (anisotropy factor for quartz 0.795) and the highest stress (at crack tip). During the first sealing event (Fig. 4i-I) the crystal fragments of the blue grain quickly reconnect (fast c-axis), whereas the slow growing m-faces of the red grain interact with the lateral expanding m-faces of the blue grain and form a bump/c-shape radiator (Fig. 4i-II). When this specimen is refractured in the vein center the c-shape radiator increases (Fig. 4k), whereas when the second initial crack is inserted in the top half of the vein a second c-shape radiator forms during fracture sealing.

3.2. Effect of fracture aperture

In this section we show the effect of varying fracture aperture on the crystal morphology in a multi-grain setup. Here, a polycrystalline rock (1200x300Δx comprising 100 grains) is generated with a Voronoi tessella-

tion and a randomly distributed crystal orientation (Fig. 5a). Here, and in the forthcoming sections we compute between four to eight crack-seal events, which captures the essential microstructures in natural veins at reasonable computational costs. Similar as in the previous section an initial crack (length 25Δx) is inserted at the left boundary of the domain and a mode I loading condition is applied. The fracture propagates anisotropically through the polycrystalline host rock while leaving a rough crack profile (Fig. 5b-d). In the first case (Fig. 5d and 6a), the fully fractured rock is opened vertically to an aperture of 40Δx ($0.8\,\mathrm{D_m}$) and the sealing is initiated (Fig. 6b) To close the crack, the broken grains reconnect and form an ataxial type of vein structure as introduced in Figure 1.

In the next sections we indicate with $\mathrm{D_m}$ the average diameter of quartz grains in host rocks, which can be used for scaling and comparison of the numerical results to different types of quartz rich host rocks.

The procedure of fracturing and sealing is repeated five times (crack-seal events), whereas the respective seed of the new crack is inserted randomly on the left boundary after the vein is fully sealed (Fig. 6b-f). We observe the formation of stretched crystals with a broad spectrum of grain boundary structures (radiator microstructures). Depending on the crystallographic orientation of a grain and its neighboring grains and where a new fracture cuts through the vein, either flat, c- or s-shape grain boundaries form as in the previous section. Refractured unfavorably orientated crystals (fast growing c-axis horizontally oriented; blue and red colored grains) are out-competed by more favorably oriented crystals (green colored grains) and do not reconnect anymore. When a non-joining crystal is refractured again a crystal inclusion

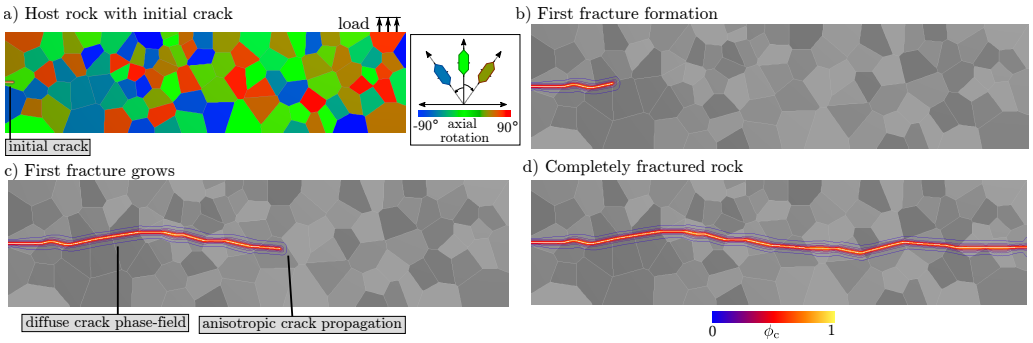

Figure 5: Fracture formation in polycrystalline quartz microstructure. a) Initial host rock structure with randomly oriented grains. Color bar indicates axial tilt of each grain. Initial crack is inserted on left side. b)-d) Fracture propagates through host rock and follows crystallographic orientations. The isolines of the diffuse crack phase-field are highlighted in color on the grayish host rock for better visibility.

forms, where the crystal is totally surrounded by other crystals and is isolated in the vein (Fig. 6e). The various types of sealing events are indicated and named in Figure 6f.

Additionally to the previous aperture ($0.8\,D_m$) we vary the opening increment and test 0.4, 1.6, 3.2, and $6.4\,D_m$ (constant in each series). For the aperture of $6.4\,D_m$ (four crack-seal events) we observe both a zig-zag shaped crack path and an inhomogeneous crystal growth front during the first crack-seal event. During the sealing favorably oriented crystals reconnect fast (similar as in Fig. 4c,i) and terminate unfavorably oriented crystals by growth competition and form mostly flat or c-shape radiators (Fig. 7a). For this aperture crystal inclusions/fragments as documented in natural ataxial vein morphologies are also found when refracturing is close to the host rock/vein boundary where misoriented crystals are present (3^{rd} sealing in Fig. 7b). In

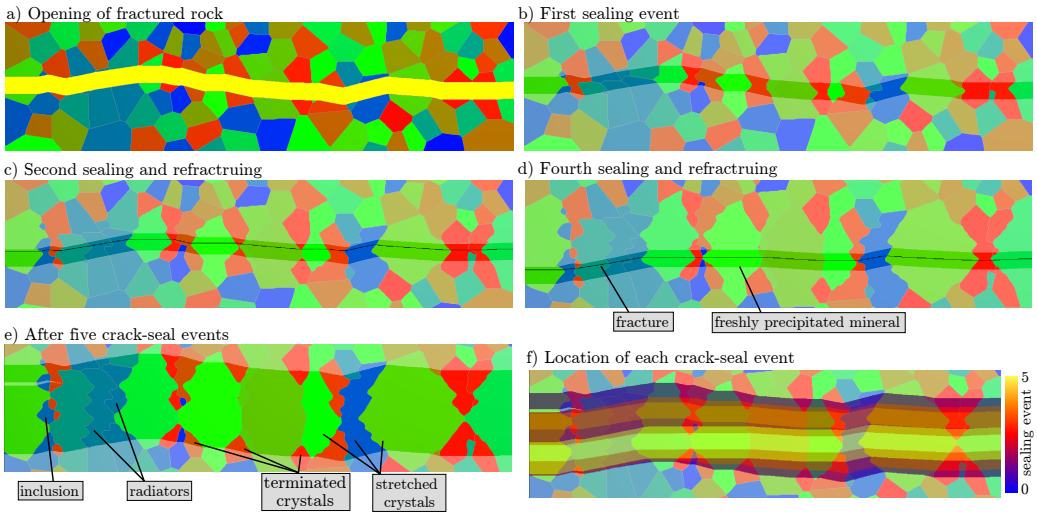

Figure 6: a) Fluid filled fractured rock from Fig. 5 is opened. Liquid phase in yellow. b) First sealing event with freshly precipitated quartz highlighted in darker color (opening increment $0.8\,D_m$). c)-e) show second, fourth, and fifth crack-seal event. New fracture is indicated with black line and in e) initial host rock is highlighted in white. f) shows which part of the vein developed in which sealing event.

the fourth crack-seal event the crystals exposed to the liquid phase (in yellow) are mostly vertically aligned (greenish grains), which results in a flat crack path and also in a more homogeneous growth front compared to the first crack-seal event (Fig. 7c).

In the small aperture ($0.4\ D_m$) we observe no preferred crystal orientation in vein center after eight crack-seal events (Fig. 8a,b). In this case the small aperture leaves little space for crystallographic oriented growth competition, also resulting in less pronounced radiators and few inclusion bands as in Figure 6.

For an increasing aperture the serrated grain boundaries become more pronounced, as long as unfavorably grains are still present ($1.6\,D_m$ in Fig. 8c,d).

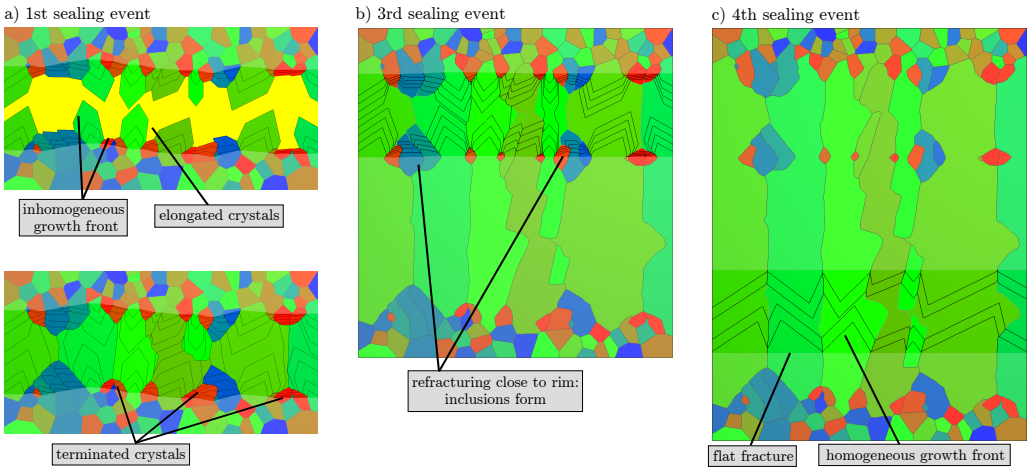

Figure 7: Crack-seal simulation with an aperture of $6.4\,D_m$. a) First sealing event: Top row shows intermediate stage with elongated crystals. Bottom row shows fully sealed vein. Black lines indicate intermediate growth stages and the precipitated minerals are highlighted in brighter color. Fully sealed vein after b) third and c) fourth sealing event with inclusions and a homogeneous growth front.

When the fracture opening further increases, misoriented grains are terminated early (close to the rim) and only fast growing grains are present ($3.2\,D_m$ in Fig. 8e,f) with lesser serrated grain boundaries. The crystallographic preferred orientation (CPO) from the rim to vein center increases with larger aperture (Fig. 8g) and the crystal width within the veins also increases with larger apertures from similar sized crystals (for $0.4\,D_m$) to a factor of four (for $6.4\,D_m$).

3.3. Accessory minerals

Quartz-rich metasediments contain porosity and minerals such as feldspars, calcite or mica. In this section we show the effect of varying composition of

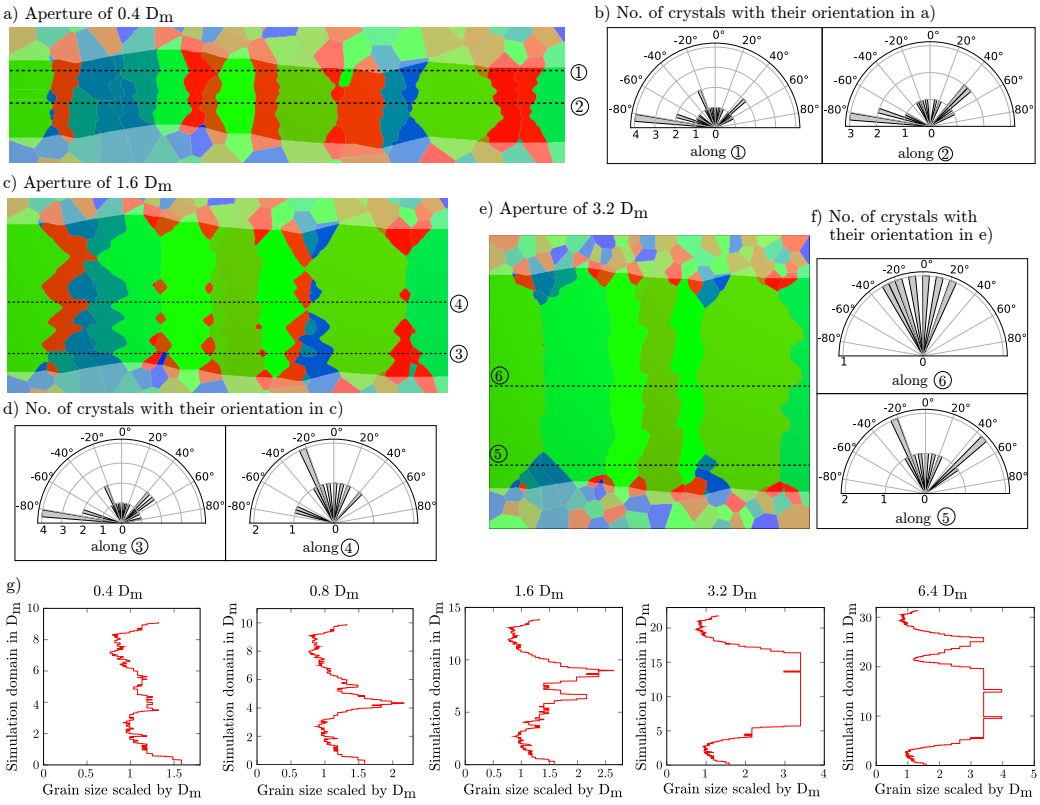

Figure 8: Evolution of crystallographic preferred orientations: Fully sealed vein with opening increment of a) 0.4 D_m (seven crack-seal events), c) 1.6 D_m (five crack-seal events), and e) 3.2 D_m (five crack seal events) with rose diagrams of crystal orientations along profile lines 1, 2 in b), 3, 4 in d), and 5, 6 in f). g) Crystal widths measured in fully sealed veins. Therefore, the computational vein was horizontally sliced, the number of grains were counted and then the domain width was divided by the counted grains.

accessory minerals in the host rock on the vein crystal morphology. We vary the percentage of secondary minerals in this section from 0-40%. Since the aqueous solution in the open fracture is assumed to be supersaturated with respect to quartz only the secondary minerals do not grow. Therefore, we set the mobility of accessory minerals to all other occurring phases to zero. In

the fracture formation models, the elastic properties of the inert grains correspond to a feldspar (albite: E=88.8GPa ν=0.25 (Pabst et al. (2015))) and the fracture resistance of the albite grains is set isotropic to half the value of quartz (similar ratio as in (Hogan et al. (2012))) for the sake of simplicity.
The initial numerical host rock structures are depicted in the top rows of Figure 9a-c with randomly distributed crystallographic orientations (150 grains, 1200x450Δx). The staggered crack-seal procedure is the same as in the previous sections. However, here the insertion of the initial crack is also allowed in the host rock close to the vein and the random position of the initial cracks are set in all three cases at the same position (previously determined) for a direct comparability.
Similar as in Section 3.2 the fracture propagates anisotropically in the quartz grains and cuts straight through the albite grains due to the chosen isotropic crack resistance. During the sealing of the open fracture no epitaxial precipitation occurs on the inert grains. This results in wider quartz crystals within the vein compared to pure quartz host rock in Fig. 9a since the quartz crystal expand laterally over their neighboring albite grains (radiator archetype *inert neighbor*). Even unfavorably oriented crystals are more likely to survive with an increasing amount of accessory minerals present (Fig. 9a-c) as they experience less growth competition in their immediate vicinity due to the presence of the inert minerals. This also results in fewer surviving and more wider crystals inside the vein with an increasing number of inert grains (Fig. 9d-e) as previously reported in in bi-mineralic quartz systems (Becker et al. (2011)) or in limestones (Spruženiece et al. (2021, 2020); Späth et al. (2021)).

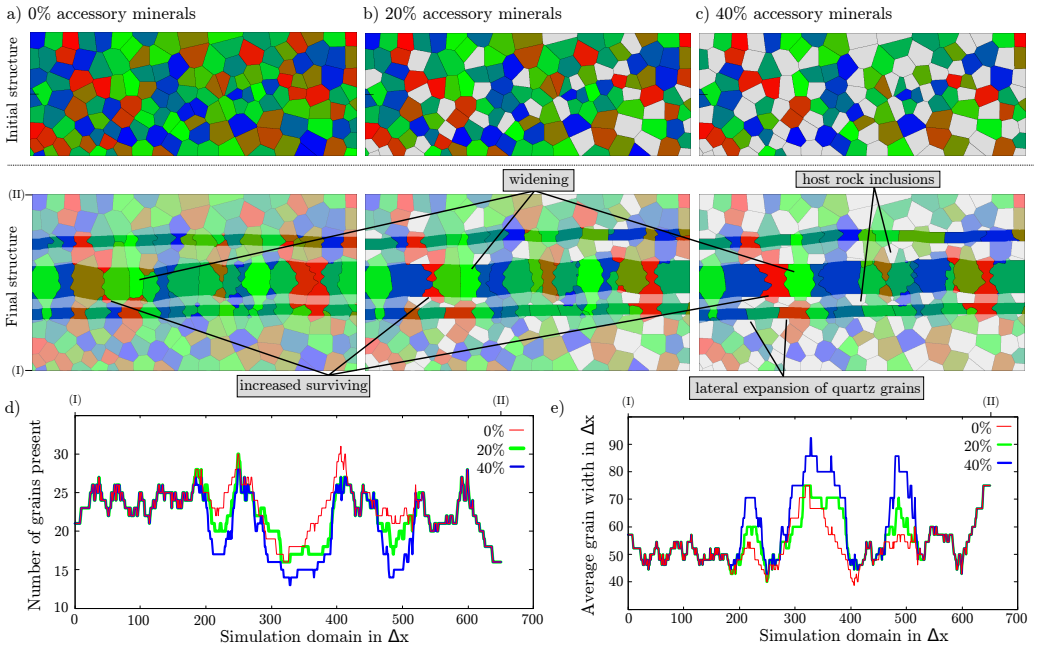

Figure 9: Variation of accessory minerals (albite) of a) 0%, b) 20%, and c) 40%. The inert albite grains are marked in gray. In a)-c) the top row shows the initial host rock and the bottom row the fully sealed veins (opening increment $0.8\,D_m$). d) Number of grains present and e) average grain width in fully sealed veins (measured in horizontally cut slices from (I) to (II) in a)).

3.4. Oblique opening trajectory

In the previous sections a mode I loading condition in vertical direction was applied in the fracture formation simulations. Here we explore the effect of oblique opening trajectories on the crystal morphology and test the cases of (I) refracturing of fully sealed veins and (II) refracturing of partially sealed veins.

In case (I) an initial crack is inserted in the upper left side of the quartz host rock. Then, the structure is loaded at an angle of 45°, 30°, and 15°

to the vertical axis (Fig. 10a-c). As expected, an inclined fracture propagation is observed due to the tensile and shear components of the loading (u_x and u_y). The fracture path is influenced by the direction of the stress state (perpendicular to lowest principle stress) and anisotropic fracture resistance. After the structure is fully fractured the rock structure below the fracture is shifted downwards in loading direction to a vertical aperture of $0.8\,D_m$ (as in Fig. 6). After the opening of the fracture a part on the right side of the simulation domain is cut off since the simulation setup and crack formation is non-periodic and the structure below the fracture is shifted to the left (which leaves an empty space on the bottom right).

Similarly as in the previous sections fractured crystals reconnect and serrated grain boundaries and crystal inclusions form. With an increased degree of shearing the stretched vein crystals exhibit an increased axial tilt after five crack-seal events, whereas the crystals are oriented in opening direction. Additionally, we measure the angle of the host rock/vein interface (wall rock normal vector), which indicates the direction of the fracture path and observe different angles between opening and wall rock normal vector due to the difference of the direction of the lowest principle stress and opening vector.

In contrast to case (I) of Section 3.4 the refracturing of partially sealed veins is investigated in case (II). We treat the two scenarios: (II-a) and (II-b). In the first scenario, the opening vector trajectory is constant, whereas in the second scenario the opening vector trajectory varies in different crack-seal events.

For the first subcase (II-a) we apply the same opening vector/trajectory (30^o) in all simulations. After the first cracking of the quartz host rock (ini-

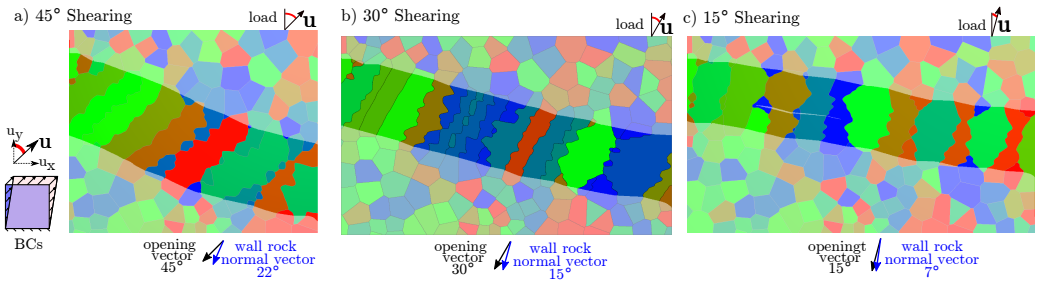

Figure 10: Oblique opening of fully sealed veins with angles of a) 45°, b) 30°, and c) 15°. The applied displacement boundary conditions (BCs) are depicted on left in a) and the angle of displacement load **u** to the vertical direction is highlighted in red on top of each image. On bottom: The opening and wall rock normal vector show the difference between applied shearing/opening trajectory (and how the crystal fragments follow this direction) and the (average) normal vector of the vein/host rock interface. The vertical opening increment is $0.8\,D_m$.

tial crack on the top left side in Fig. 11a) and the first sealing we initiate the new refracturing (after same time step in all iterations) once favorably oriented crystal fragments have reconnected, whereas the misoriented crystals have not touched and leave a porous space in the vein (Fig. 11b). The new fracture cuts through the vein crystals which results in the formation of either elongated isolated crystal bridges (where pores are between reconnecting crystals) or laterally connected bridges (little pores in between reconnecting crystal) which is depicted Figure 11c. This mechanism of the formation of elongated and isolated crystal bridges has been previously reported and is in agreement with the work of Lander and Laubach (2015). After five crack-seal events the crystal growth of the partial filled vein is continued until the fracture is fully sealed (Fig. 11c). In contrast to case (I) very few radiator structures and more flat grain boundaries are visible in this vein. The lat-

erally connected bridges (on right) show serrated grain boundaries due to repeated refracturing and growth competition with their crystal neighbors in each event, whereas the isolated crystal bridges (on left) laterally expand over their misoriented neighbors during the complete sealing and form flat radiators where their m-facets meet (Fig. 11d). Similar as in case (I) opening and wall rock normal vector differ.

In case (II-b) a mode-I loading is applied during the first fracturing event

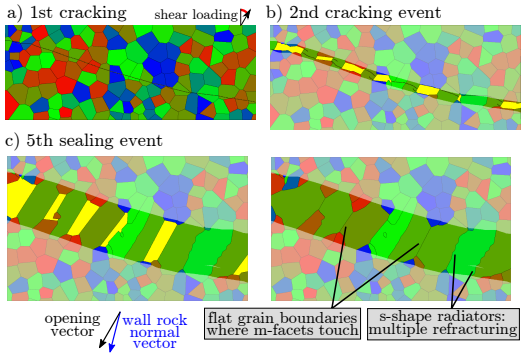

Figure 11: Oblique opening of partially sealed fractures with a constant opening trajectory, where the vertical opening increment is $0.8\,\mathrm{D_m}$. a) First cracking in host rock. The direction of loading is indicated with an arrow (same boundary conditions as in Fig. 10). b) Porous structure with few reconnected crystals is refractured. c) Crystal bridges in partial sealed vein (left) and different crystal morphologies in fully sealed fracture (left).

resulting in a flat fracture (Fig. 12a). Then similar as in case (II-a) the opening vector is set to 30° and a refracturing is initiated once the first crystals reconnected (Fig. 12b), which results in similar crystal structures as in case (II-a). Since the vein is weaker than the host rock (as in Virgo et al. (2013)) the fracture localizes inside the open fracture (and not in the host rock). The localization point of the crack depends on how far the neighboring crystals

of the bridged crystals grow into the open fracture (Fig. 12c). If a neighboring crystal grows slowly (e.g. second, third, sixth line from left in Fig. 12c) the localization point is close to the rim, however if the neighboring grain grows fast (e.g. first, fourth, fifth line from left in Fig. 12c) the crystal bridge fractures further away from the vein/host rock interface. In contrast to case (I) (Fig. 10) and case (II-a) (Fig. 11), after six crack-seal events the angle between the opening and wall rock normal vectors is nearly the same angle as the applied shear loading (Fig. 12d).

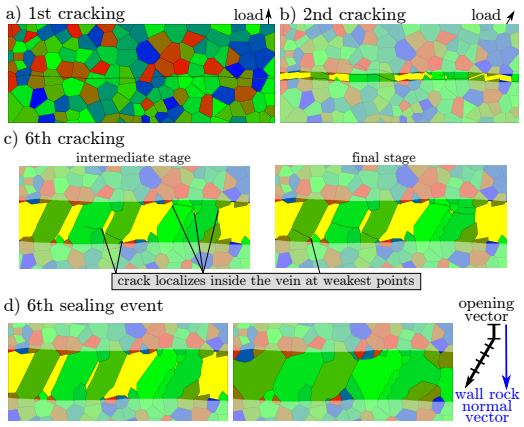

Figure 12: Oblique opening of partially sealed veins with a varying opening trajectory. The vertical opening increment in each step is $0.8\,D_m$. a) First fracture in host rock under mode I loading. b) Refracturing of partially sealed vein with an oblique loading. c) Sixth fracturing event in intermediate (left) and final stage (right). The crack localizes inside the vein at the bridges where the stress is the highest. d) Sixth sealing event: Crystal bridges occur in partially sealed structures (left). Fully sealed vein (on right) with flat and serrated grain boundaries.

4. Discussion

This study serves as a first-time development of a sequential and uniform simulation of the combined cracking and sealing processes of quartz microstructures. We built upon and expand previous works of Becker et al. (2011); Spruženiece et al. (2021); Nollet et al. (2005); Lander and Laubach (2015); Späth et al. (2021); Ankit et al. (2015); Prajapati et al. (2020) which discussed influencing factors on the crystal morphologies of veins, where our study is in general agreement with these previous works. The present work showcases a systematic study giving novel insights in the formation of different radiator archetypes and vein microstructures under a broad range of boundary conditions (e.g. opening trajectory, host rock composition). Additionally, this study is one of the very first which is able to show how the fracture path is influenced by the evolution of the precipitated crystals, since the fracturing and sealing process are solved sequentially.

The crystal morphologies in natural veins show a broad spectrum of shapes. In order to elucidate these complex structures we first analysed the formation of different archetypes of serrated grain boundaries and categorized them in three characteristic cases by computing two competing crystals in a sealing event. In contrast to the previous work of Urai et al. (1991), which explained the formation of serrated grain boundaries with an isotropic growth model and oblique openings (which implies no radiators under pure mode I opening), the present work reveals that for the formation of radiator structures an anisotropic (crystalline) growth is necessary to obtain serrated grain boundaries in both normal and shear openings (as in Ankit et al. (2015)). The in-

troduced phase-field model indicates, that the shape of the radiators depend on the orientation of a crystal and its neighboring crystals in combination with aperture size, location of refracturing, and if the neighboring grains are inert. However, there might be further factors affecting the growth competition during the formation of serrated grain boundaries like the presence of several growing minerals (Becker et al. (2011)) or coatings on grain surfaces, which results in a reduced growth velocity at those nucleation discontinuities (e.g. (Lander et al. (2008); Okamoto and Sekine (2011); Busch et al. (2021))).

In most of the presented simulations an initial crack is randomly set in the computational rock structure inside an existing vein, which leads to thick multi-crack-seal veins. This artificial fracture initialization corresponds to a fracture localization at a weaker spot or pore outside of the simulation domain inside the vein. For a better prediction of the crack paths and the resulting crystal morphology, additional factors on the location of a crack initiation could be incorporated in future works as, for example, porous host rocks, or stress inhomogeneities (due to different mineralogies). Furthermore, we assumed that the grain boundaries have the same strength as the host rock grains and vein crystals, which results in transgranular cracking. This is commonly the case for quartzites which were well compacted and are quite pure. However, in cases of weaker grain boundaries preferential intergranular fracturing should be incorporated (e.g. as in (Prajapati et al. (2020))) to extend future works to different types of quartz rich rocks. Including those factors could then enable the description of crack-seal (localized) and crack-jump (delocalized fracturing) veins and predict a criterion for the transition

of those mechanisms. Moreover, for a more precise comparison between the numerical veins to natural rock systems further data is necessary as opening vector/trajectory, chemical composition, pressure, and temperature of fluid. Then, additionally studies with varying opening increments and trajectories could provide a better understanding of vein structures which formed under a complex stress state.

Due to the sequential simulative approach of cracking and sealing both processes influence each other. The crack path depends on the crystal structure of the previous sealing events and the crystal growth depends on the previous cracking events and as a consequence the crack path can change during the iterations (e.g. Fig. 7). Especially in the simulations of partially sealed structures (Fig. 11, 12) the incorporation of simulative cracking is essential since the crack localizes at the weakest position of the vein (might be at rim or center). We expect that the choice of a predetermined artificial crack path will result in different microstructures (non-preferential grains get cut) and an accurate prediction of the factors affecting the vein morphology might be erroneous. Therefore the simulative approach of fracturing seems necessary to draw accurate conclusions on the formation mechanism of natural veins from the simulated veins.

In the simulations with an oblique opening vector the stretched crystals followed the opening trajectory (high tracking efficiency), since the aperture increment was small compared to the host rock grain size (0.8 D_m), which is similar as in antitaxial veins (Urai et al. (1991); Hilgers et al. (2001)). How-

ever, we expect that for larger opening increments fewer crystals fragments reconnect and follow the opening trajectory and at some point form a median line in the vein center. Future studies could additionally test, for example, effects of larger shearing angles and indicate when crystals do not reconnect anymore.

The discussed numerical studies are performed exclusively in 2D to limit computational costs for the fracturing and sealing in a polycrystalline rock structure. In principle the presented phase-field models is applicable in 3D, albeit higher computational costs (especially the mechanical calculations). Even though 3D simulations enable a more heterogeneous crystallographic orientation (3D rotation vs. in-plane rotation in 2D) and automatically incorporate the out-of plane growth we expect that our findings can be transferred and are valid in 3D. This validity of 2D cases showing similar and consistent structures than 3D results has been demonstrated by previous phase-field studies (Spruženiece et al. (2021); Späth et al. (2021); Ankit et al. (2015)). However, when the permeability and fluid connectivity of open fractures is of interest 3D simulations are essential (Paluszny et al. (2020); Kling et al. (2017)).

The phase-field models support the understanding of serrated grain boundaries with complex crystal shapes and structures and provide insights in the textural development of stretched crystals. In Figure 13 we compare exemplary representative numerical crystal structures to natural veins from Portugal near Almograve and Carrapateira. Our results are in visually convincing

agreement with the natural rocks while showing many similar features as, for example, flat and serrated grain boundaries, lateral expansion of quartz grains over accessory minerals, and sheared crystals. Furthermore, our studies show a similar behavior as hydrothermal quartz growth experiments, like crystallographically oriented growth competition, lateral expansion of favorably oriented crystals or overgrowth of accessory minerals (Okamoto and Sekine (2011); Busch et al. (2021)).

The phase-field method is able to give accurate predictions under various boundary conditions and is capable to reproduce a wide range of natural crystal structures. Therefore, characteristic features can be determined in natural veins to draw conclusions on the formation mechanisms by comparing them to the numerical veins. For example the crystal width and the amount of grain boundary serration inside the vein give a hint on the aperture increment. A larger crystal width and a more serrated grain boundary with more space between the radiators indicates a larger aperture (Fig. 8). Additionally the occurrence of numerous crystal inclusions (isolated crystals) inside the whole vein implies a small to medium aperture in a vein with a high sealing state when refracturing starts. In contrast, when the crystal morphology shows mostly flat grain boundaries, early refracturing of a partially sealed vein is likely to occur (bridge structure) as observable in Figure 11.

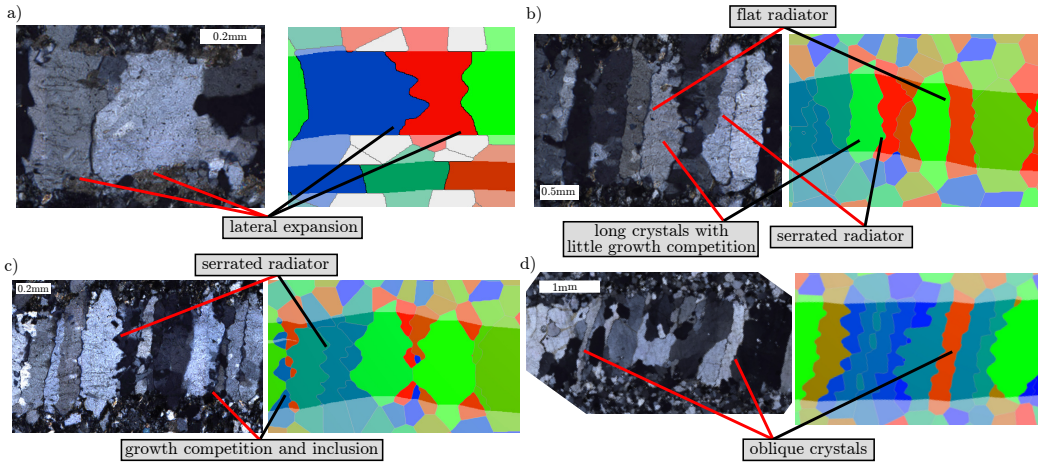

Figure 13: Comparison of phase-field simulations to natural veins in quartz microstructures. Light microscopic image with crossed polarizers of all natural veins from Portugal near Carrapateira (CA) and near Almograve (AL). a) Lateral expansion of quartz crystals over accessory mineral forming wide vein crystals in quartzite near CA. b) and c) showing characteristic features of multi-crack-seal veins in quartzite near CA with stretched crystals as flat and serrated grain boundaries resulting from growth competition. d) Vein with oblique crystals in quartzite near AL.

5. Concluding remarks

The present work showcases the versatility and capability of the multiphase-field method in modeling fracture sealing processes, where different crystallographic anisotropies are included in the models of both fracturing and sealing. A systematic phase-field study on the formation of multi-crack-seal veins in quartz microstructures is presented, where we show the effects of different factors on the crystal morphology as aperture, accessory minerals, and oblique opening trajectories of fully and partially sealed fractures. The simulated structures show many similarities with natural veins in quartz microstructures and give valuable insight in the crack-seal mechanism. Our

work is in general agreement by also further expanding previous studies of vein formation (Lander and Laubach (2015); Ankit et al. (2015); Wendler et al. (2016)).

Our results reveal that

- the shape of a serrated grain boundary depends on the crystallographic orientation of a grain and its neighboring grains and on the location of a new refracturing event. In a two grain system three different archetypes of radiators are observed: (i) flat (ii) c-shape and (iii) s-shape.

- with small fracture apertures little growth competition between the fractured grains occurs, which is resulting in no crystallographic preferred orientation (CPO) inside the vein. With an increasing aperture increment growth competition is possible and leads to larger crystal width with a CPO inside the vein.

- quartz grains laterally expand over accessory minerals when they are exposed to the fracture surface while forming wider crystals compared to pure quartz host rocks. This produces another type of radiator: (iv) inert neighbor.

- the sealing state of the open fracture impacts the grain boundary shape. In fully sealed veins with a small aperture ($0.8\,D_m$) radiators form, whereas refractured porous structures tend to show more flat grain boundaries.

Acknowledgments

We thank German Research Foundation DFG for funding the main parts of the modeling and simulation research work within the project (NE 822/34-1, UR 64/17-1). Support for the numerical solution has been contributed through the program "MTET: 38.04.04" of the Helmholtz association. We thank Liene Spruženiece for providing the micrographs. The constructive reviews of C. Hilgers, of an anonymous reviewer and the editorial handling of Stefano Mazzoli are appreciated. JLU acknowledges funding by EU ITN FLUIDNET project. JLU acknowledges the support of a Theodore von Karman fellowship and the hospitality of Stefan Schmalholz during a sabbatical at the University of Lausanne where the first steps of this project were made. The authors acknowledge support by the state of Baden-Württemberg through bwHPC.

References

S. F. Cox, M. Etheridge, V. Wall, The role of fluids in syntectonic mass transport, and the localization of metamorphic vein-type ore deposists, Ore Geology Reviews 2 (1987) 65–86.

R. H. Sibson, F. Robert, K. H. Poulsen, High-angle reverse faults, fluid-pressure cycling, and mesothermal gold-quartz deposits, Geology 16 (1988) 551–555.

D. D. McNamara, A. Lister, D. J. Prior, Calcite sealing in a fractured geothermal reservoir: Insights from combined EBSD and chemistry mapping, Journal of Volcanology and Geothermal Research 323 (2016) 38–52.

A. Almansour, S. E. Laubach, J. E. Bickel, R. A. Schultz, Value-of-Information Analysis of a Fracture Prediction Method, SPE Reservoir Evaluation & Engineering 23 (2020) 0811–0823. doi:10.2118/198906-PA.

J. G. Ramsay, M. I. Huber, The Techniques of Modern Structural Geology. Volume 1: Strain Analysis, Academic Press, London, 1983.

C. W. Passchier, R. A. J. Trouw, Microtectonics, Springer Science & Business Media, 2005.

S. E. Laubach, R. H. Lander, L. J. Criscenti, L. M. Anovitz, J. L. Urai, R. Pollyea, J. N. Hooker, W. Narr, M. A. Evans, S. N. Kerisit, et al., The role of chemistry in fracture pattern development and opportunities to advance interpretations of geological materials, Reviews of Geophysics 57 (2019) 1065–1111.

A.-M. Boullier, F. Robert, Palaeoseismic events recorded in Archaean gold-quartz vein networks, Val d'Or, Abitibi, Quebec, Canada, Journal of Structural Geology 14 (1992) 161–179.

D. M. Fisher, S. L. Brantley, Models of quartz overgrowth and vein formation: deformation and episodic fluid flow in an ancient subduction zone, Journal of Geophysical Research: Solid Earth 97 (1992) 20043–20061.

S. F. Cox, Structural and isotopic constraints on fluid flow regimes and fluid pathways during upper crustal deformation: an example from the Taemas area of the Lachlan Orogen, SE Australia, Journal of Geophysical Research: Solid Earth 112 (2007).

P. D. Bons, M. A. Elburg, E. Gomez-Rivas, A review of the formation of tectonic veins and their microstructures, Journal of Structural Geology 43 (2012) 33–62.

J. G. Ramsay, The crack–seal mechanism of rock deformation, Nature 284 (1980) 135–139.

R. Caputo, P. L. Hancock, Crack-jump mechanism of microvein formation and its implications for stress cyclicity during extension fracturing, Journal of Geodynamics 27 (1998) 45–60.

M. Holland, J. L. Urai, Evolution of anastomosing crack–seal vein networks in limestones: Insight from an exhumed high-pressure cell, Jabal Shams, Oman Mountains, Journal of Structural Geology 32 (2010) 1279–1290.

S. Virgo, S. Abe, J. L. Urai, The evolution of crack seal vein and fracture networks in an evolving stress field: Insights from Discrete Element Models of fracture sealing, Journal of Geophysical Research: Solid Earth 119 (2014) 8708–8727.

D. W. Durney, J. G. Ramsay, Incremental strains measured by syntectonic crystal growths, in: K. A. De Jong, R. Scholten (Eds.), Gravity and tectonics, Wiley, New York, 1973, pp. 67–96.

S. Becker, C. Hilgers, P. A. Kukla, J. L. Urai, Crack-seal microstructure evolution in bi-mineralic quartz–chlorite veins in shales and siltstones from the RWTH-1 well, Aachen, Germany, Journal of Structural Geology 33 (2011) 676–689.

R. H. Lander, R. E. Larese, L. M. Bonnell, Toward more accurate quartz cement models: The importance of euhedral versus noneuhedral growth rates, AAPG Bulletin 92 (2008) 1537–1563.

L. Spruženiece, M. Späth, J. L. Urai, E. Ukar, M. Selzer, B. Nestler, Wide-blocky veins explained by dependency of crystal growth rate on fracture surface type: Insights from phase-field modeling, Geology (2021). doi:10.1130/G48472.1.

L. Spruženiece, M. Späth, J. L. Urai, E. Ukar, M. Selzer, B. Nestler, A. Schwedt, Formation of wide-blocky calcite veins by extreme growth competition, Journal of the Geological Society (2020). doi:10.1144/jgs2020-104.

F. Renard, M. Andréani, A.-M. Boullier, P. Labaume, Crack-seal patterns: Records of uncorrelated stress release variations in crustal rocks, in: D. Gapais, J. P. Brun, P. R. Cobbold (Eds.), Deformation Mechanisms, Rheology and Tectonics: from Minerals to the Lithosphere, volume 243, Geological Society (London) Special Publication, 2005, pp. 67–79.

L. A. Thomas, N. Wooster, W. A. Wooster, The hydrothermal synthesis of quartz, Discussions of the Faraday Society 5 (1949) 341–345.

C. B. Cecil, M. T. Heald, Experimental investigation of the effects of grain coatings on quartz growth, Journal of Sedimentary Research 41 (1971) 582–584.

A. Okamoto, H. Saishu, N. Hirano, N. Tsuchiya, Mineralogical and textural variation of silica minerals in hydrothermal flow-through experiments: im-

plications for quartz vein formation, Geochimica et Cosmochimica Acta 74 (2010) 3692–3706.

A. Okamoto, K. Sekine, Textures of syntaxial quartz veins synthesized by hydrothermal experiments, Journal of Structural Geology 33 (2011) 1764–1775. doi:https://doi.org/10.1016/j.jsg.2011.10.004.

B. Busch, A. Okamoto, K. Garbev, C. Hilgers, Experimental fracture sealing in reservoir sandstones and its relation to rock texture, Journal of Structural Geology 153 (2021) 104447. doi:https://doi.org/10.1016/j.jsg.2021.104447.

J. L. Urai, P. Williams, H. Van Roermund, Kinematics of crystal growth in syntectonic fibrous veins, Journal of Structural Geology 13 (1991) 823–836.

J. Zhang, J. B. Adams, FACET: a novel model of simulation and visualization of polycrystalline thin film growth, Modelling and Simulation in Materials Science and Engineering 10 (2002) 381.

P. D. Bons, Development of crystal morphology during unitaxial growth in a progressively widening vein: I. The numerical model, Journal of Structural Geology 23 (2001) 865–872.

C. Hilgers, D. Koehn, P. D. Bons, J. L. Urai, Development of crystal morphology during unitaxial growth in a progressively widening vein: II. Numerical simulations of the evolution of antitaxial fibrous veins, Journal of Structural Geology 23 (2001) 873–885.

S. Nollet, J. L. Urai, P. D. Bons, C. Hilgers, Numerical simulations of polycrystal growth in veins, Journal of Structural Geology 27 (2005) 217–230.

R. H. Lander, S. E. Laubach, Insights into rates of fracture growth and sealing from a model for quartz cementation in fractured sandstones, GSA Bulletin 127 (2015) 516–538.

J. F. W. Gale, R. H. Lander, R. M. Reed, S. E. Laubach, Modeling fracture porosity evolution in dolostone, Journal of Structural Geology 32 (2010) 1201–1211.

P. Hartman, W. G. Perdok, On the relations between structure and morphology of crystals. I, Acta Crystallographica 8 (1955) 49–52.

S. Virgo, S. Abe, J. L. Urai, Extension fracture propagation in rocks with veins: Insight into the crack-seal process using Discrete Element Method modeling, Journal of Geophysical Research: Solid Earth 118 (2013) 5236–5251.

S. Virgo, S. Abe, J. L. Urai, The influence of loading conditions on fracture initiation, propagation, and interaction in rocks with veins: Results from a comparative Discrete Element Method study, Journal of Geophysical Research: Solid Earth 121 (2016) 1730–1738.

X. Zhang, R. G. Jeffrey, Role of overpressurized fluid and fluid-driven fractures in forming fracture networks, Journal of Geochemical Exploration 144 (2014) 194–207.

X. Wang, F. Shi, C. Liu, D. Lu, H. Liu, H. Wu, Extended finite element simulation of fracture network propagation in formation containing frictional and cemented natural fractures, Journal of Natural Gas Science and Engineering 50 (2018) 309–324.

Y. D. Ha, F. Bobaru, Studies of dynamic crack propagation and crack branching with peridynamics, International Journal of Fracture 162 (2010) 229–244.

A. Paluszny, R. N. Thomas, M. C. Saceanu, R. W. Zimmerman, Hydromechanical interaction effects and channelling in three-dimensional fracture networks undergoing growth and nucleation, Journal of Rock Mechanics and Geotechnical Engineering 12 (2020) 707–719.

M. Mohammadnejad, H. Liu, A. Chan, S. Dehkhoda, D. Fukuda, An overview on advances in computational fracture mechanics of rock, Geosystem Engineering (2018) 1–24.

Z. Xu, P. Meakin, Phase-field modeling of solute precipitation and dissolution, The Journal of Chemical Physics 129 (2008) 014705.

N. Ray, J. Oberlander, P. Frolkovic, Numerical investigation of a fully coupled micro-macro model for mineral dissolution and precipitation, Computational Geosciences 23 (2019) 1173–1192.

C. Bringedal, L. von Wolff, I. S. Pop, Phase field modeling of precipitation and dissolution processes in porous media: Upscaling and numerical experiments, Multiscale Modeling & Simulation 18 (2020) 1076–1112.

N. Prajapati, M. Späth, L. Knecht, M. Selzer, B. Nestler, Quantitative Phase-Field Modeling of Faceted Crystal Dissolution Processes, Crystal Growth & Design 21 (2021) 3266–3279.

N. Prajapati, M. Selzer, B. Nestler, Computational modeling of calcite cementation in saline limestone aquifers: a phase-field study, Geothermal Energy 5 (2017) 15.

M. Späth, L. Spruženiece, J. L. Urai, M. Selzer, M. Arndt, B. Nestler, Kinematics of crystal growth in single-seal syntaxial veins in limestone - a phase-field study, Journal of Geophysical Research: Solid Earth (2021). doi:https://doi.org/10.1029/2021JB022106.

N. Prajapati, M. Selzer, B. Nestler, B. Busch, C. Hilgers, Modeling fracture cementation processes in calcite limestone: a phase-field study, Geothermal Energy 6 (2018) 7.

K. Ankit, J. L. Urai, B. Nestler, Microstructural evolution in bitaxial crack-seal veins: A phase-field study, Journal of Geophysical Research: Solid Earth 120 (2015) 3096–3118.

F. Wendler, A. Okamoto, P. Blum, Phase-field modeling of epitaxial growth of polycrystalline quartz veins in hydrothermal experiments, Geofluids 16 (2016) 211–230.

N. Prajapati, M. Selzer, B. Nestler, B. Busch, C. Hilgers, K. Ankit, Three-dimensional phase-field investigation of pore space cementation and permeability in quartz sandstone, Journal of Geophysical Research: Solid Earth 123 (2018) 6378–6396.

N. Prajapati, A. Abad Gonzalez, M. Selzer, B. Nestler, B. Busch, C. Hilgers, Quartz Cementation in Polycrystalline Sandstone: Insights From Phase-

Field Simulations, Journal of Geophysical Research: Solid Earth 125 (2020) e2019JB019137.

M. Ambati, T. Gerasimov, L. De Lorenzis, Phase-field modeling of ductile fracture, Computational Mechanics 55 (2015) 1017–1040.

C. Miehe, F. Aldakheel, A. Raina, Phase field modeling of ductile fracture at finite strains: A variational gradient-extended plasticity-damage theory, International Journal of Plasticity 84 (2016) 1–32.

T.-T. Nguyen, J. Réthoré, J. Yvonnet, M.-C. Baietto, Multi-phase-field modeling of anisotropic crack propagation for polycrystalline materials, Computational Mechanics 60 (2017) 289–314.

N. Prajapati, C. Herrmann, M. Späth, D. Schneider, M. Selzer, B. Nestler, Brittle anisotropic fracture propagation in quartz sandstone: insights from phase-field simulations, Computational Geosciences (2020) 1–16.

T. T. Nguyen, J. Bolivar, Y. Shi, J. Réthoré, A. King, M. Fregonese, J. Adrien, J.-Y. Buffiere, M.-C. Baietto, A phase field method for modeling anodic dissolution induced stress corrosion crack propagation, Corrosion Science 132 (2018) 146–160.

A. Mikelić, M. F. Wheeler, T. Wick, Phase-field modeling of a fluid-driven fracture in a poroelastic medium, Computational Geosciences 19 (2015) 1171–1195.

M. Ambati, T. Gerasimov, L. De Lorenzis, A review on phase-field models of brittle fracture and a new fast hybrid formulation, Computational Mechanics 55 (2015) 383–405.

Y. Heider, A review on phase-field modeling of hydraulic fracturing, Engineering Fracture Mechanics 253 (2021) 107881.

J. Cahn, S. Allen, A microscopic theory for domain wall motion and its experimental verification in Fe-Al alloy domain growth kinetics, Le Journal de Physique Colloques 38 (1977) C7–51.

A. A. Griffith, VI. The phenomena of rupture and flow in solids, Philosophical Transactions of the Royal Society of London. Series A, Containing Papers of a Mathematical or Physical Character 221 (1921) 163–198. doi:10.1098/rsta.1921.0006.

G. A. Francfort, J.-J. Marigo, Revisiting brittle fracture as an energy minimization problem, Journal of the Mechanics and Physics of Solids 46 (1998) 1319–1342.

M. Norton, B. Atkinson, Stress-dependent morphological features on fracture surfaces of quartz and glass, Tectonophysics 77 (1981) 283–295.

C. C. Ferguson, G. E. Lloyd, R. J. Knipe, Fracture mechanics and deformation processes in natural quartz: a combined Vickers indentation, SEM, and TEM study, Canadian Journal of Earth Sciences 24 (1987) 544–555.

C. Kuhn, R. Müller, A continuum phase field model for fracture, Engineering Fracture Mechanics 77 (2010) 3625–3634.

C. Miehe, F. Welschinger, M. Hofacker, Thermodynamically consistent phase-field models of fracture: Variational principles and multi-field FE implementations, International Journal for Numerical Methods in Engineering 83 (2010) 1273–1311.

D. Schneider, E. Schoof, Y. Huang, M. Selzer, B. Nestler, Phase-field modeling of crack propagation in multiphase systems, Computer Methods in Applied Mechanics and Engineering 312 (2016) 186–195.

P. Heyliger, H. Ledbetter, S. Kim, Elastic constants of natural quartz, The Journal of the Acoustical Society of America 114 (2003) 644–650.

B. Nestler, H. Garcke, B. Stinner, Multicomponent alloy solidification: phase-field modeling and simulations, Physical Review E 71 (2005) 041609.

I. Steinbach, Phase-field models in materials science, Modelling and Simulation in Materials Science and Engineering 17 (2009) 073001.

J. Hötzer, A. Reiter, H. Hierl, P. Steinmetz, M. Selzer, B. Nestler, The parallel multi-physics phase-field framework Pace3D, Journal of Computational Science 26 (2018) 1–12.

V. Goldschmidt, Atlas der Kristallformen, volume 7, C. Winter, 1922.

W. Pabst, E. Gregorova, E. Rambaldi, M. C. Bignozzi, Effective elastic constants of plagioclase feldspar aggregates in dependence of the anorthite content: a concise review, Ceramics-Silikaty 59 (2015) 326–330.

J. D. Hogan, R. J. Rogers, J. G. Spray, S. Boonsue, Fracture and fragmentation of quartz and albite during single-diamond sliding-point contact, Engineering Fracture Mechanics 96 (2012) 165–178.

T. Kling, J.-O. Schwarz, F. Wendler, F. Enzmann, P. Blum, Fracture flow due to hydrothermally induced quartz growth, Advances in Water Resources 107 (2017) 93–107.